

Sensing Rotations with Multiplane Light Conversion

M. Eriksson¹, A.Z. Goldberg^{1,2,3}, M. Hiekkämäki¹, F. Bouchard,² J. Rehacek⁴, Z. Hradil^{5,6,*}, G. Leuchs^{5,6}, R. Fickler¹, and L.L. Sánchez-Soto^{1,5,7,*}

¹Physics Unit, Photonics Laboratory, Tampere University, Tampere 33720, Finland

²National Research Council of Canada, 100 Sussex Drive, Ottawa, Ontario K1N 5A2, Canada

³Department of Physics, University of Ottawa, 25 Templeton Street, Ottawa, Ontario K1N 6N5, Canada

⁴Department of Optics, Palacky University, 17. Listopadu 12, Olomouc 77146, Czech Republic

⁵Max-Planck-Institut für die Physik des Lichts, Erlangen 91058, Germany

⁶Department of Physics, Friedrich-Alexander-Universität Erlangen-Nürnberg, Erlangen 91058, Germany

⁷Departamento de Óptica, Facultad de Física, Universidad Complutense, Madrid 28040, Spain

(Received 30 January 2023; revised 9 June 2023; accepted 4 August 2023; published 21 August 2023)

We report an experiment estimating the three parameters of a general rotation. The scheme uses quantum states attaining the ultimate precision dictated by the quantum Cramér-Rao bound. We realize the states experimentally using the orbital angular momentum of light and implement the rotations with a multiplane light-conversion setup, which allows one to perform arbitrary unitary transformations on a finite set of spatial modes. The observed performance suggests a range of potential applications in the next generation of rotation sensors.

DOI: 10.1103/PhysRevApplied.20.024052

I. INTRODUCTION

Rotation sensors are indispensable elements for numerous applications. Examples include inertial navigation [1,2], geophysical studies [3], and tests of general relativity [4–6], and significant technological progress is opening alternative potential uses. As diverse as the applications are, the repertoire of available sensors has continued to grow: from small MEMS gyros [7], over fiber-optic gyros [8] and electrochemical devices [9–11], to high-resolution ring lasers [12,13] and matter-wave interferometers [14–16].

These technological advances are boosting the performance to levels where quantum effects come into play [17]. Therefore, it seems pertinent to analyze the ultimate limits of rotation sensors from a quantum perspective.

The problem of determining all three parameters defining a rotation constitutes a paradigmatic example of a multiparameter estimation. This encapsulates the confluence between measuring incompatible observables and

achieving the ultimate precision limits. Quantum metrology promises that certain probe states and measurement procedures can dramatically outperform standard (classical) protocols to simultaneously estimate multiple parameters with the ultimate precision [18–22].

The optimal probe states for sensing arbitrary rotations are known as Kings of Quantumness [23–25] (initially dubbed anticoherent states [26]). These probes have the remarkable property that their low-order moments of key observables are *unchanged* via rotations, instead imprinting rotation information in higher-order moments. As well, through the Majorana representation [27], they exhibit highly symmetric geometrical structures on the Poincaré (or Bloch) sphere, which can be used to intuit their metrological properties [28–30]. These probe states have previously been generated with orbital angular momentum (OAM) carrying light modes to demonstrate single-parameter estimation [31] and, recently, also in intrinsic polarization degrees of freedom [32].

Given an optimal probe state subject to an unknown rotation, what measurement scheme best reveals the rotation parameters? Although there might be an ideal positive operator-valued measure (POVM) that may never be easily realized in a realistic system, we can aptly ask where it can be approximated with straightforward measurements. The answer is positive: just like a globe can be oriented by finding the locations of London and Tokyo, so, too, can a quantum state be oriented by measuring its projections onto a small number of axes pointed at various directions

*lsanchez@fis.ucm.es

Published by the American Physical Society under the terms of the [Creative Commons Attribution 4.0 International license](#). Further distribution of this work must maintain attribution to the author(s) and the published article's title, journal citation, and DOI. Open access publication funded by the Max Planck Society.

on the surface of the sphere. This scheme was outlined in Ref. [33] and is now demonstrated.

We generate our ideal probe states in the OAM basis by using spatial light modulators (SLMs). This basis comprises a high-dimensional state space. These states then undergo rotations by passing through a multiplane light converter (MPLC) [34,35], which is capable of enacting arbitrary linear transformations using a series of phase modulations with free-space propagation between each of the planes. The rotated states are then projected onto coherent states oriented along various axes; from these data, we can reconstruct all of the rotation parameters.

This paper is organized as follows. In Sec. II, we briefly review some basic properties of rotations and their effects. In Sec. III, we discuss the ultimate limits in rotation sensing and derive the optimal states for that task. In Sec. IV we present the details of our experimental setup, while, in Sec. V, we analyze the obtained results. Finally, our conclusions are summarized in Sec. VI.

II. PRELIMINARIES ABOUT ROTATIONS

In general, a rotation is characterized by three parameters [36]: either the two angular coordinates of the rotation axis and the angle rotated around that axis, or a trio of Euler angles. We follow the former option throughout and consider a rotation of angle ω and rotation axis $\mathbf{u}(\Theta, \Phi) = (\sin \Theta \cos \Phi \quad \sin \Theta \sin \Phi \quad \cos \Theta)^\top$, where the superscript T denotes the transpose. We will use the compact notation $\boldsymbol{\Omega}(\omega, \mathbf{u}) = (\omega, \Theta, \Phi)$ to denote these angles. It is well known that the action of this rotation in Hilbert space is represented by [37]

$$R(\boldsymbol{\Omega}) = e^{i\omega \mathbf{J} \cdot \mathbf{u}}, \quad (1)$$

where we have used the standard angular momentum notation \mathbf{J} for the generators, which satisfy the commutation relations of the Lie algebra $\mathfrak{su}(2)$: $[J_x, J_y] = iJ_z$ and circular permutations thereof (with $\hbar = 1$ throughout this work).

We consider the $(2J + 1)$ -dimensional space \mathcal{H}_J , spanned by the states $\{|J, m\rangle\}$, with $m = -J, \dots, +J$. This is the Hilbert space of spin- J particles, but also describes the case of symmetric combinations of $2J$ qubits. Indeed, via the Jordan-Schwinger representation [38,39], which represents the algebra $\mathfrak{su}(2)$ in terms of bosonic amplitudes, the space \mathcal{H}_J also encompasses many different instances of two-mode problems, such as, e.g., polarization, strongly correlated systems, and Bose-Einstein condensates [40] with fixed total numbers of excitations. Actually, one can consider the spin J as a proxy for the input resources required in a metrological setting and inspect the precision of various estimates in terms of J , with a goal of maximizing precision for an estimate while minimizing J . In what follows, we assume that we work in \mathcal{H}_J . This

restriction is reasonable since maximal precision will be obtained by concentrating all of the resources into a single subspace corresponding to the average total number of particles.

The notion of Majorana constellations [27] will prove to be extremely convenient for our purposes. In this representation, a pure state corresponds to a configuration of points on the Bloch sphere, a picture that makes a high-dimensional Hilbert spaces easier to comprehend. The idea can be presented in a variety of ways [41,42], but the most direct one is, perhaps, by first recalling that SU(2)-or Bloch-coherent states can be defined as rotated versions of a fiducial state [43,44]

$$|z\rangle \equiv |\mathbf{n}\rangle = \frac{1}{(1 + |z|^2)^J} \exp(zJ_+) |J, -J\rangle, \quad (2)$$

where $J_\pm = J_x \pm iJ_y$ are ladder operators and $z = \exp(-i\phi) \tan(\theta/2)$, which corresponds to a stereographical projection from the south pole, mapping the point $z \in \mathbb{C}$ to the point of spherical coordinates (θ, ϕ) fixing the unit vector \mathbf{n} . Coherent states are precisely eigenstates of the operator $\mathbf{J} \cdot \mathbf{n}$ and they constitute an overcomplete basis. So, every pure state $|\psi\rangle \in \mathcal{H}_J$ can be expanded in that basis as

$$\psi(z^*) = \langle z|\psi\rangle = \frac{1}{(1 + |z|^2)^J} \sum_{m=-J}^J \binom{2J}{J+m}^{1/2} \psi_m z^{J+m}, \quad (3)$$

where $\psi_m = \langle J, m|\psi\rangle$ are the amplitudes of the state in the angular momentum basis. Since this is a polynomial, $|\psi\rangle$ is determined by the set $\{z_i\}$ of the $2J$ complex zeros of $\psi(z)$. A nice geometrical representation of $|\psi\rangle$ by $2J$ points on the unit sphere (often called the Majorana constellation) is obtained by an inverse stereographic map $\{z_i\} \mapsto \{\theta_i, \phi_i\}$.

Let us examine a few examples to illustrate how this representation works in practice. The first one is that of SU(2) or Bloch coherent states $|\mathbf{n}_0\rangle$, for which the constellation collapses in this case to a single point diametrically opposed to \mathbf{n}_0 .

For the angular momentum basis, $|J, m\rangle$ can be easily inferred from the polynomial so they consist of $J \pm m$ stars at the north and south poles, respectively.

Another relevant set of states are the NOON states [45]

$$|\text{NOON}\rangle = \frac{1}{\sqrt{2}}(|J, J\rangle - |J, -J\rangle), \quad (4)$$

for which the Majorana constellations have $2J$ stars placed around the equator of the Bloch sphere with equal angular separation between each star.

Since the most classical states (i.e., coherent states) have the most concentrated constellations, one might intuitively

think that the most quantum states have their $2J$ stars distributed most symmetrically on the unit sphere, and this is the case. This constitutes the realm of the Kings of Quantumness [23,24]. In a sense they are the opposite of Bloch coherent states, as they *point nowhere*; in other words, the average angular momentum vanishes and the fluctuations up to given order M are isotropic [28–30]. Their symmetrical Majorana constellations herald their isotropic angular momentum properties and give an intuitive picture that these states are the most sensitive for rotation measurements.

III. ESTIMATING ROTATION PARAMETERS

A typical rotation measurement requires the vector Ω to be imprinted on a (preferably pure) probe state $|\psi\rangle$, in which the latter is shifted by applying a corresponding rotation $R(\Omega) \in \text{SU}(2)$ that encodes the three parameters Ω . A set of measurements is then performed on the output state $|\psi_\Omega\rangle = R(\Omega)|\psi\rangle$, with the measurements denoted by a POVM [46] $\{\Pi_x\}$, where the POVM elements are labeled by an index x that represents the possible outcomes of the measurement according to Born's rule $p(x|\Omega) = \langle\psi_\Omega| \Pi_x |\psi_\Omega\rangle$. From these outcomes, we infer the vector parameter via an estimator $\widehat{\Omega}$ [47].

The performance of the estimator is assessed in terms of the covariance matrix $\mathbf{C}_\psi(\widehat{\Omega})$, defined as

$$[\mathbf{C}_\psi(\widehat{\Omega})]_{jk} = \langle (\widehat{\Omega}_j - \Omega_j)(\widehat{\Omega}_k - \Omega_k) \rangle, \quad (5)$$

where $j, k \in (1, 2, 3)$ and the expectation value is taken with respect to the probability distribution $p(x|\Omega)$. The diagonal elements are the variances, the nondiagonal elements characterize the correlations between the estimated

parameters, and an ideal estimator will minimize this covariance matrix for some fixed amount of resources.

The ultimate limit for any possible POVM is given by the quantum Cramér-Rao bound (QCRB), which promises that [48]

$$\mathbf{C}_\psi(\widehat{\Omega}) \succcurlyeq \mathbf{Q}_\psi^{-1}(\Omega), \quad (6)$$

where matrix inequalities $\mathbf{A} \succcurlyeq \mathbf{B}$ mean that $\mathbf{A} - \mathbf{B}$ is a positive semidefinite matrix. Here, the lower bound is the inverse of the quantum Fisher information matrix (QFIM), which takes the particularly simple form for pure states and unitary evolution [19]

$$[\mathbf{Q}_\psi(\Omega)]_{jk} = 4\mathbf{C}_\psi(G_j, G_k). \quad (7)$$

The operators G_j are the generators of the transformation, determined through $G_j = iR^\dagger(\Omega)\partial_{\Omega_j}R(\Omega)$, and the symmetrized covariance between two operators is $\mathbf{C}_\psi(A, B) = \frac{1}{2}\langle AB + BA \rangle - \langle A \rangle \langle B \rangle$, with the expectation values taken with respect to the original state $|\psi\rangle$. The QFIM grows as $\mathbf{Q} \rightarrow v\mathbf{Q}$ when an experiment is repeated v independent times, so we hereafter take $v = 1$ to inspect the ultimate sensitivity bounds per experimental trial.

Computing these generators requires some subtlety, due to the noncommutativity $[\partial_{\Omega_k}(\mathbf{J} \cdot \mathbf{u}), \mathbf{J} \cdot \mathbf{u}] \neq 0$. Following the approach in Ref. [49] (see also the alternative method in [50]), one gets a compact expression for the QFIM:

$$\mathbf{Q}_\psi(\Omega) = 4\mathbf{H}^\top(\Omega) \mathbf{C}_\psi(\mathbf{J}) \mathbf{H}(\Omega), \quad (8)$$

where $\mathbf{H}(\Omega) = (\mathbf{h}_\omega \quad \mathbf{h}_\Theta \quad \mathbf{h}_\Phi)^\top$ with

$$\mathbf{h}_\omega = -\mathbf{u},$$

$$\mathbf{h}_\Theta = \begin{pmatrix} -\sin\omega\cos\Theta\cos\Phi - \cos\omega\sin\Phi + \sin\Phi & (\cos\omega - 1)\cos\Phi - \sin\omega\cos\Theta\sin\Phi & \sin\omega\sin\Theta \end{pmatrix}^\top, \quad (9)$$

$$\mathbf{h}_\Phi = \begin{pmatrix} \sin\omega\sin\Theta\sin\Phi + \sin^2\frac{1}{2}\omega\sin 2\Theta\cos\Phi & \sin^2\frac{1}{2}\omega\sin 2\Theta\sin\Phi - \sin\omega\sin\Theta\cos\Phi & -2\sin^2\frac{1}{2}\omega\sin^2\Theta \end{pmatrix}^\top,$$

and $[\mathbf{C}_\psi(\mathbf{J})]_{jk} = \mathbf{C}_\psi(J_j, J_k)$. Notably,

$$\mathbf{H}^\top(\Omega)\mathbf{H}(\Omega) = \begin{pmatrix} 1 & 0 & 0 \\ 0 & 4\sin^2\frac{1}{2}\omega & 0 \\ 0 & 0 & 4\sin^2\frac{1}{2}\omega\sin^2\Theta \end{pmatrix}. \quad (10)$$

The remarkable property of these expressions is that we have separated the parameter dependence, contained in $\mathbf{H}(\Omega)$ from the state dependence that is embodied in $\mathbf{C}_\psi(\mathbf{J})$. To find states optimally suited for estimating arbitrary unknown rotations one must optimize $\mathbf{C}_\psi(\mathbf{J})$, which

has been dubbed as the *sensitivity covariance matrix*. The most classical states have the smallest sensitivity covariance matrix, to the point of being singular, while the most quantum states have the largest sensitivity covariance matrix.

Given a covariance matrix, we can balance the precision of the various parameters by using a weight matrix $\mathbf{W} \succ 0$. In this way, the QCRB leads to the scalar inequality

$$\text{Tr}[\mathbf{W}\mathbf{C}_\psi(\widehat{\Omega})] \geq \text{Tr}[\mathbf{W}\mathbf{Q}_\psi^{-1}(\Omega)]. \quad (11)$$

The left-hand side is the so-called weighted mean square error of the estimator, whereas the right-hand side plays

the role of a cost function. For a given \mathbf{W} , the standard approach is to minimize this cost. Following Ref. [49], we take the weight matrix to be the SU(2) metric $\mathbf{W} = \mathbf{H}^\top \mathbf{H}$, which remarkably cancels with the \mathbf{H} matrices determining the QFIM, so that the QCRB becomes

$$\text{Tr}[\mathbf{C}_\psi^{-1}(\mathbf{J})] \geq \frac{9}{J(J+1)}. \quad (12)$$

The trace of the inverse achieves the minimum only when the state is first- and second-order unpolarized; that is, $\langle \mathbf{J} \rangle = 0$ and $\mathbf{C}_\psi(\mathbf{J}) \propto \mathbb{1}$. This is precisely the case for the Kings of Quantumness.

The saturability of the QCRB is a touchy business. For pure states, the QCRB can be saturated if and only if $\text{Im}\langle \psi_\Omega | L_j L_k | \psi_\Omega \rangle = 0$, where L_j is the symmetric logarithmic derivative respect to the j th parameter [19]. This hinges upon the expectation values of the commutators of the generators. Fortunately, for states with isotropic covariance matrices, the expectation values of the commutators are guaranteed to vanish. In fact, these expectation values will vanish for all states that are first-order unpolarized. The Kings thus guarantee that all three parameters can be simultaneously estimated at a precision saturating the QCRB for any triad of rotation parameters.

The measurement saturating the QCRB has been recently characterized in terms of a POVM with elements that are projections onto $|\psi_\Omega\rangle$ and the three states proportional to $(\mathbf{J} \cdot \mathbf{h}_i)|\psi_\Omega\rangle$ [33]. However, its experimental implementation may be challenging. Easier is to project the rotated state onto a set of Bloch coherent states for various directions and to reconstruct the rotation parameters from these measurements.

The set of continuous projections

$$\mathcal{Q}_{\mathbf{n}} = |\langle \mathbf{n} | \psi_\Omega \rangle|^2 \quad (13)$$

constitute the Husimi function [52]. Knowledge of all of the projections $\mathcal{Q}_{\mathbf{n}}$ is equivalent to knowledge of the rotated state $|\psi_\Omega\rangle$, but such information is redundant: it suffices to sample the function at a few locations $\mathcal{Q}_{\mathbf{n}}$ and use these results to orient the Husimi function and thus estimate the rotation parameters.

At how many locations must the Husimi function be sampled to uniquely orient it? In general, the answer depends on the probe state and the locations being sampled. Using the same basic principles applied to geographical positioning systems (GPS) [53], we argued in Ref. [33] that five projections should be more than enough for this orientation problem.

We first choose an arbitrary Bloch coherent state $|\mathbf{n}_1\rangle$ onto which we project the rotated state $|\psi_\Omega\rangle$, which amounts to sampling the Husimi function at \mathbf{n}_1 . We take this to be the state $|J, J\rangle$. The value of $\mathcal{Q}_{\mathbf{n}_1}$ defines a set of level curves, and the state *must* be oriented in such a way

that \mathbf{n}_1 lies on one of these curves. Rotating the state along any of these level curves will produce the same value $\mathcal{Q}_{\mathbf{n}_1}$. In the analogy in the introduction, such a level curve is akin to pinpointing the location of London, with the rest of the globe free to rotate about that point. But, since the analogy breaks down because more than one point on the sphere may have the same value of the Husimi function, we must contend with multiple possible level curves at this stage.

To remove some of this ambiguity, we next, project the rotated state onto another coherent state $|\mathbf{n}_2\rangle$ to define another set of level curves. We take this next state to be the opposite coherent state $|J, -J\rangle$. Rotating the state along these level curves again produces the same value $\mathcal{Q}_{\mathbf{n}_2}$, so in general we expect there to be multiple *intersection points* for orienting the Husimi function such that \mathbf{n}_1 lies along a curve $\mathcal{Q}_{\mathbf{n}_1}$ and \mathbf{n}_2 lies along a curve $\mathcal{Q}_{\mathbf{n}_2}$. For the introductory analogy of orienting London and Tokyo, this would suffice, but the existence of multiple level curves means our work is not complete.

In all but pathological cases, a third projection uniquely specifies one of the above intersection points for orienting the Husimi function. We include a fourth projection to deal with pathological cases and a fifth projection to help with normalization, where more and more projections provide redundant information that will make the overall measurement more precise. We take these projections to be onto three coherent states pointing toward the equator, first \mathbf{n}_3 in the y direction, then \mathbf{n}_4 in the x direction, and finally \mathbf{n}_5 in the $\sqrt{2}x + y$ direction. Put in different words, the set of d angular coordinates \mathbf{n}_i can be rigidly rotated until the d projections $\mathcal{Q}_{\mathbf{n}_i}$ match the given state $|\psi_\Omega\rangle$. The pathological cases are those for which the projections match the given state rotated by different sets of rotation parameters.

IV. EXPERIMENT

To verify the proposed method, we use an experimental setup sketched in Fig. 1. It consists of three sections: state generation, unitary manipulation, and state measurement. Different $4f$ imaging systems, which were omitted from the figure, are used to connect the sections. We use a cw diode laser (Roithner RLT808-100G, $\Delta\lambda = 2$ nm) at a central wavelength of 810 nm, and phase-only SLMs (Holoeye Pluto-2) along with standard free-space optical components to perform the experiment. For accurate phase modulations, we also perform aberration correction for all phase screens using a Gerchberg-Saxton phase-retrieval algorithm [54].

First, we encode the probe state $|\psi\rangle$ in the transverse spatial degree of freedom of a laser beam; in other words, Laguerre-Gauss modes LG_l^p carrying OAM of light, emerging from a single-mode fiber by displaying a phase and amplitude modulating mask on the first SLM [55] with an added Gaussian correction [56,57]. The chosen states are Kings of Quantumness: we consider here

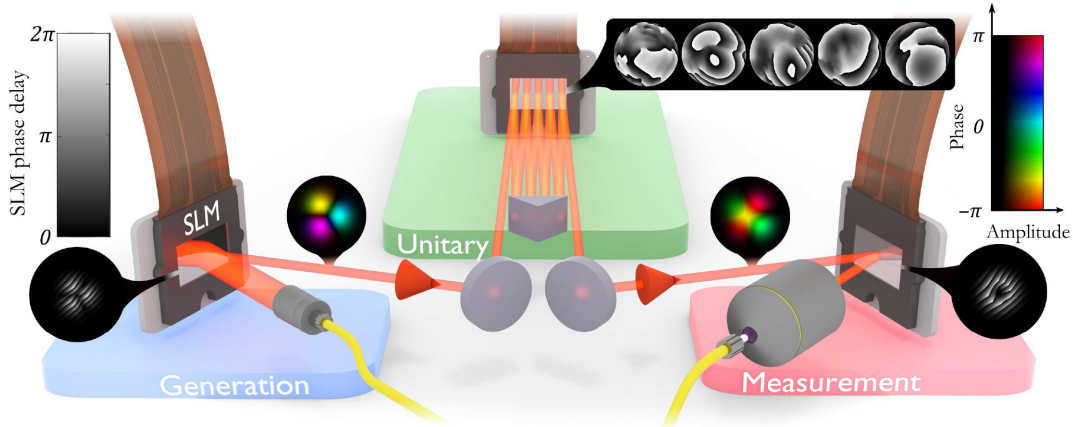


FIG. 1. A simplified sketch of the experimental system. Three SLM screens are used to perform the three steps of the experiment. The first one transforms the Gaussian beam coming out of a single mode fiber (SMF, yellow) into the desired King state that is then rotated using a unitary operation implemented through MPLC on the second SLM. The third SLM performs a projective measurement onto a state by first applying a phase and amplitude modulating mask and then coupling the beam into an SMF using a $10 \times$ microscope objective [51]. Nonmagnifying $4f$ lens systems imaging each SLM onto the next one are omitted from the figure. The shown insets correspond to field structures (in color) and phase mask structures (in gray scale). The field structure insets show a $J = 2$ King state light field on the left and a rotated version of the same King-state field structure on the right. The measurement mask filters for one of the chosen coherent states in this state space. In the image, the grating terms have been removed from the phase masks of the unitary and only the field structure at the first-diffraction orders from each phase mask are shown.

the $J = 2$ state (with a tetrahedral constellation) that lives in a five-dimensional Hilbert space

$$|\psi\rangle = \sqrt{\frac{2}{3}}|2, -1\rangle + \sqrt{\frac{1}{3}}|2, 2\rangle \quad (14)$$

and the $J = 3$ state (with a square-based pyramid and its reflection as constellation) that lives in a seven-dimensional Hilbert space

$$|\psi\rangle = \frac{1}{\sqrt{2}}(|3, -2\rangle - |3, 2\rangle). \quad (15)$$

These modes are encoded in the LG basis by generating superpositions of LG_l^p modes with radial index $p = 0$ and azimuthal indices $l = m$ (the quantum number in the state $|J, m\rangle$), which is the only degree of freedom once the spin J is set), with a beam waist of $w = 0.52$ mm. The state is then imaged onto the first phase screen of an MPLC system, which consists of five consecutive phase modulations separated by 800 mm of free-space propagation implemented using a single SLM screen [58]. The MPLC system is capable of performing an arbitrary unitary mapping between spatial modes [59], using phase modulations calculated through a wave-front-matching algorithm [60]. Here, the MPLC is used to realize the unitary transformations $R(\Omega)$ of the probe state $R(\Omega)|\psi\rangle = |\psi_\Omega\rangle$, i.e., rotations of the state. The rotations do not necessarily correspond to a physical rotation of the transverse-field structure, but rather to a rotation in the high-dimensional state space. The form of the rotations is set by J , which enforces the Hilbert space to which the LG modes are

restricted. Physically, this corresponds to a complex transformation of the transverse field dictated by the specific modes used to build up the state space. An exemplary field mask structure for enacting the rotation is depicted in Fig. 1. After the MPLC, the rotated state is imaged onto the measurement SLM, which is used along with an SMF to perform projective measurements of the rotated probe state $\mathcal{Q}_n = |\langle n|\psi_\Omega\rangle|^2$.

The raw data of the projective measurements consists of power values with different measurement settings. In the ideal case, the projective measurement is simply given by

$$\mathcal{Q}_n = |\langle n|\psi_\Omega\rangle|^2 = \frac{P_{\langle n|\psi_\Omega\rangle}}{P_{\langle\psi_\Omega|\psi_\Omega\rangle}}, \quad (16)$$

where $P_{\langle n|\psi_\Omega\rangle}$ is the power coupled to the SMF when projecting the rotated probe state $|\psi_\Omega\rangle$ onto the Bloch coherent state $|n\rangle$, and $P_{\langle\psi_\Omega|\psi_\Omega\rangle}$ is the total power readout when projecting the rotated probe state onto itself, taking into account the efficiency of the measurement.

However, in our projective measurement scheme, the power that is coupled to the SMF is highly dependent on the state being generated and projected on. To account for this, we must measure and compensate for these state-dependent detection efficiencies η . To measure the detection efficiencies of the Bloch coherent states, we make use of the following scheme. We generate the Bloch coherent state with the first SLM, and image the state through the system unaltered (setting MPLC to perform an identity unitary). Then, we measure the power projected onto

the Bloch coherent state itself $P_{\langle \mathbf{n} | \mathbf{n} \rangle}$, and the total power of the beam before the final SLM $P_{\mathbf{n}}$, giving us an efficiency measure $\eta_{\mathbf{n}} = P_{\langle \mathbf{n} | \mathbf{n} \rangle} / P_{\mathbf{n}}$. For the detection efficiencies of the rotated probe states $\eta_{\psi_{\Omega}}$, we make use of a similar scheme, but instead of imaging the state through the system unaltered, we generate a probe state $|\psi\rangle$ with the first SLM, rotate the state using the MPLC $R(\Omega)|\psi\rangle = |\psi_{\Omega}\rangle$, and measure the detection efficiency $\eta_{\psi_{\Omega}} = P_{\langle \psi_{\Omega} | \psi_{\Omega} \rangle} / P_{\psi_{\Omega}}$. With these detection efficiencies, the projective measurements are given by $\mathcal{Q}_{\mathbf{n}} = \eta_{\psi_{\Omega}} P_{\langle \mathbf{n} | \psi_{\Omega} \rangle} / (\eta_{\mathbf{n}} P_{\langle \psi_{\Omega} | \psi_{\Omega} \rangle}) = P_{\langle \mathbf{n} | \psi_{\Omega} \rangle} / (\eta_{\mathbf{n}} P_{\psi_{\Omega}})$; in other words, the fraction of the power coupled to the SMF, scaled by the efficiency of projecting onto the coherent state in question.

Each of the power values is measured as a sample mean of power data gathered for half a second, corresponding to approximately 50 datapoints. From these data, we also calculate the standard deviation for each power value, which are used to infer the standard deviations of the projective measurements via error propagation. The data for rotated $J = 2$ and $J = 3$ Kings of Quantumness, along with their standard deviations, are presented in Fig. 2. However, even after tenfold multiplication of the error bars, they are too small to be visible.

V. RESULTS

A. Axis estimation

Figure 2 shows the data for the $J = 2$ King of Quantumness state, i.e., the tetrahedron initial state, and projections onto five different coherent states for the same randomly chosen axis variables $(\Theta, \Phi) = (1.11, 3.75)$ and all rotation angles in intervals of $\pi/18$, i.e., 10 degrees. Combining all of these data for all 37 of the rotation angles, where we expect

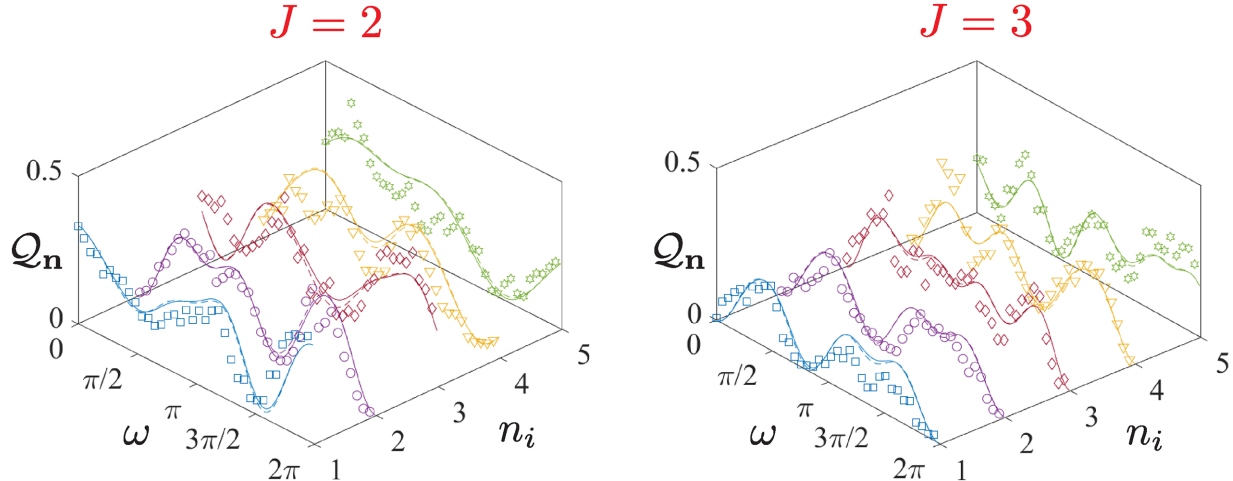


FIG. 2. Projections of the rotated $J = 2$ (left) and $J = 3$ (right) Kings of Quantumness onto five different spin coherent states. The plotted error bars are 10 times the measured standard deviations; however, in general, they are too tiny to be visible. The dashed line shows the curve obtained using the estimated rotation axis to compute $\mathcal{Q}_{\mathbf{n}_j}$, while the full line shows the theoretically expected results. The orders of the projections from 1 to 5, in terms of directions that the coherent states point on the Bloch sphere, are $+z, -z, +y, +x$, and $\sqrt{2}x + y$.

the 0 and 2π rotations to yield similar data, we can perform maximum-likelihood estimation following standard procedures [61,62]

$$(\hat{\Theta}, \hat{\Phi}) = \arg \max \sum_i \sum_{j=1}^5 \mathcal{Q}_{\mathbf{n}_j} \times \log \frac{|\langle \mathbf{n}_j | R(\omega_i, \mathbf{u}) | \psi \rangle|^2}{\sum_{i',j'} |\langle \mathbf{n}_{j'} | R(\omega_{i'}, \mathbf{u}) | \psi \rangle|^2}. \quad (17)$$

This amounts to finding a global maximum of the likelihood function (17), supplied with the experimental data $\mathcal{Q}_{\mathbf{n}_j}$, on the finite two-dimensional search space with the help of standard global optimization tools. With *no further constraints* on $0 \leq \Theta \leq \pi$ and $0 \leq \Phi < 2\pi$, the maximization procedure finds $(\hat{\Theta}, \hat{\Phi}) = (1.13, 3.79)$, immediately demonstrating the usefulness of this procedure. We note that there is a local maximum at the true variables $(1.11, 3.75)$ but this is not the global maximum. To further demonstrate the very good agreement, we also plot the estimated lines versus the true lines for coherent-state projections of the state rotated about the estimated versus the true axis in Fig. 2.

We can consider the Fisher information matrix of the estimated parameters with components

$$F_{ij} \approx \sum_{kl} \frac{\mathcal{Q}}{\mathcal{Q}_{\mathbf{n}_l}} \frac{\partial}{\partial \Omega_i} \frac{p_{kl}}{P} \frac{\partial}{\partial \Omega_j} \frac{p_{kl}}{P}, \quad (18)$$

corresponding to the amount of information per probe state and estimate the uncertainty from the inverse of the Fisher

information matrix. Here,

$$p_{kl} = |\langle \mathbf{n}_l | R(\omega_k, \mathbf{u}) | \psi \rangle|^2, \quad P = \sum_{kl} p_{kl}, \quad \mathcal{Q} = \sum_l \mathcal{Q}_{\mathbf{n}_l}, \quad (19)$$

and all of the derivatives can be computed analytically using the generators $G_j = \mathbf{J} \cdot \mathbf{h}_j$. When we do this, we find

$$\mathbf{F}^{-1}(\Theta, \Phi) = \begin{pmatrix} 0.261 & -0.0471 \\ -0.0471 & 0.452 \end{pmatrix}. \quad (20)$$

Using this inverse as the covariance matrix for the estimates of the axis parameters [62] lets us report the uncertainties in our estimates of Θ and Φ as 0.51 and 0.67, respectively. For comparison, the best possible value of the QFI for a single experiment is $\mathbf{F}_{\max} = \frac{1}{3}4J(J+1)\sin^2(\omega_i/2)\text{diag}(4, 4\sin^2\Theta)$, where $\text{diag}(\mathbf{v})$ is a square diagonal matrix with the elements of vector \mathbf{v} on the main diagonal. Averaging over the 37 different values of ω that were used, this becomes

$$\mathbf{F}_{\max}^{-1}(1.13, 3.79) = \begin{pmatrix} 0.0642 & 0. \\ 0. & 0.0786 \end{pmatrix}. \quad (21)$$

Our measured uncertainties are larger than the ultimate bounds by factors of 2.0 and 2.4 for Θ and Φ , respectively.

In the second set of experiments, we performed the same tasks for the $J = 3$ state. The true rotation angles are $(\Theta, \Phi) = (2.40, 2.76)$ and the estimated ones with no constraints are $(\Theta, \Phi) = (2.37, 2.75)$. Again, the data along with the estimated and theoretical curves are plotted in Fig. 2, showing good agreement. However, due to the increased dimension of the utilized states without an increase in phase modulation planes of the MPLC system, the performance of our experiment slightly degrades. Performing the observed Fisher information calculation yields

$$\mathbf{F}^{-1}(\Theta, \Phi) = \begin{pmatrix} 0.203 & 0.0174 \\ 0.0174 & 0.282 \end{pmatrix}, \quad (22)$$

to be compared to the theoretical minimum uncertainty given by

$$\mathbf{F}_{\max}^{-1}(2.37, 2.75) = \begin{pmatrix} 0.0321 & 0 \\ 0 & 0.0666 \end{pmatrix}. \quad (23)$$

Our measured uncertainties are larger than the ultimate bounds by factors of 2.5 and 2.1 for Θ and Φ , respectively.

We can discuss the scaling of these results with J . While there is clearly a larger Fisher information for the $J = 3$

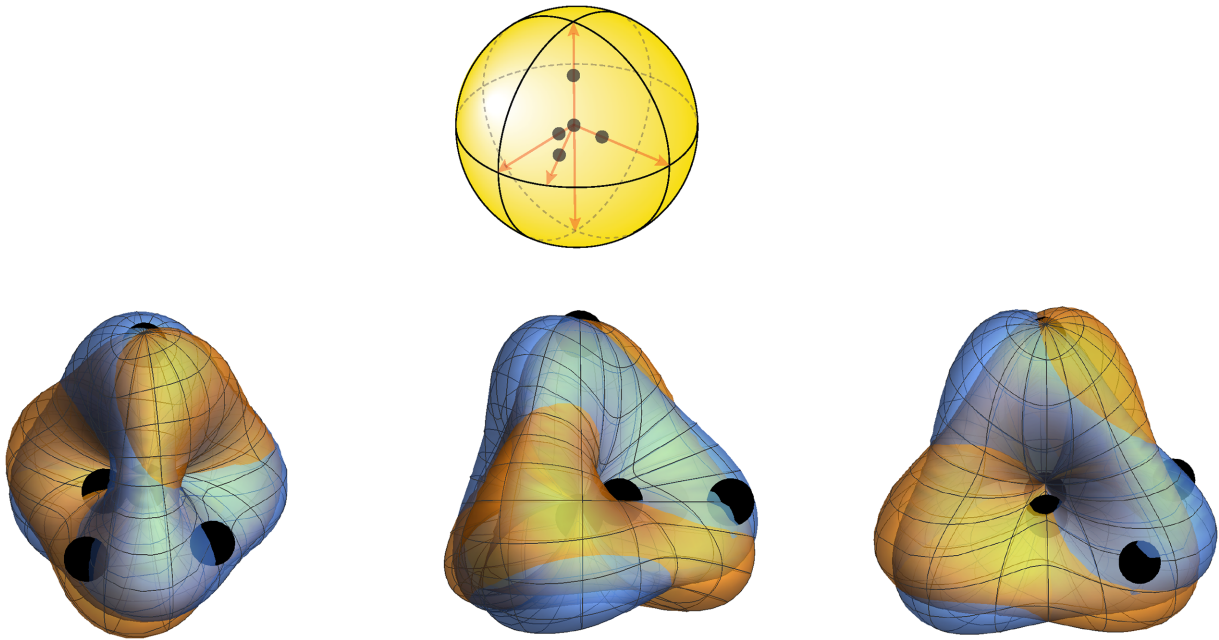


FIG. 3. Example of the true rotated state (orange surface) and estimated rotated state (blue surface) for $J = 2$ and a rotation by $\pi/18$ about a randomly chosen rotation axis. The radial coordinates are given by the magnitude of the Husimi \mathcal{Q} function. Plotted are three perspectives of this three-dimensional object, along with five black spheres at the five measured data points. The rotation estimation algorithm tries to rotate the surface until it best matches the data points, with “best” defined according to a maximum-likelihood estimation procedure. These perspectives let us visualize how well the estimated orientation matches the correct one, and the absolute orientation of the perspective is less relevant for visualization because we are interested in these relative results to inspect the performance of the algorithm. For absolute orientation, plotted on the top is a sphere to indicate how the black spheres are distributed in space.

state than the $J = 2$ state, we must be careful because the best possible QFI depends on the rotation axis. We can create a unique figure of merit by weighing the observed uncertainties by the metric $\mathbf{g} = \text{diag}(1, \sin^2 \Theta)$ and taking the trace. This finds

$$\text{Tr}(\mathbf{g}\mathbf{F}_{J=2}^{-1}) = 0.63, \quad \text{Tr}(\mathbf{g}\mathbf{F}_{J=3}^{-1}) = 0.34. \quad (24)$$

This decrease in total uncertainty with N is approximately the anticipated $1/[J(J+1)]$ scaling, which would provide a factor of 2 difference here. For comparison, the ultimate limits are $37/[48J(J+1)]$, which approximately equal 0.13 and 0.064 for $J = 2$ and $J = 3$. A NOON state, with $\mathbf{C}_\psi = \text{diag}(J/2, J/2, J^2)$ or a transposition of the diagonal elements for a NOON state in another direction, has ultimate limits in the range $0.18 - 0.22$ and $0.10 - 0.14$ for $J = 2$ and $J = 3$, respectively, for the axes chosen randomly here. Since the results remain within a factor of 3 in uncertainty of the best possible values for all J tested here, it is certainly reasonable to expect dramatic quantum advantages as J grows, at which point they will also outperform NOON states. All of these outperform SU(2)-coherent states, the most classical of states, because these cannot be used to simultaneously estimate multiple parameters of a rotation due to the singularity of their sensitivity covariance matrices.

B. Angle and axis estimation

Next, we can do this estimation 37 times to find all three rotation parameters for each specific rotation. Such an estimation cannot be done in a single trial using (classical) SU(2)-coherent states, as those are insensitive to one of the three parameters of a rotation. The maximization is the same as in Eq. (17) but removing the sums over i and i' and repeating the optimization for each value of $i = i'$:

$$\widehat{\boldsymbol{\Omega}}_i = \arg \max \sum_{j=1}^5 \mathcal{Q}_{\mathbf{n}_j} \log \frac{|\langle \mathbf{n}_j | R(\boldsymbol{\Omega}_i) | \psi \rangle|^2}{\sum_{j'} |\langle \mathbf{n}_{j'} | R(\boldsymbol{\Omega}_i) | \psi \rangle|^2}. \quad (25)$$

Again, we expect to find similar estimates for the 0 and 2π rotations.

Figure 3 depicts the optimization process geometrically for the first nonzero rotation with $J = 2$ for a rotation by $\pi/18$ (10°). The true rotated state has a particular \mathcal{Q} function that is sampled at five points, then the optimization algorithm rotates the original state until it best aligns with those five sampled points. This again amounts to finding a global maximum of the likelihood function (25), now on the finite *three*-dimensional search space with the help of standard global optimization tools. The offset between the true and estimated state as well as how closely each matches the level curves from the five data points can be inspected visually. Throughout, one can see that the \mathcal{Q} function varies dramatically with angular coordinates,

possessing tetrahedral symmetry, which is what makes this state so useful for estimating rotations.

It is cumbersome to visualize all 37 experiments for each of the tested values of J , so we require a method to aggregate the estimation results. We choose to investigate the deviation between the true rotation and the estimated rotation, quantified by the angle of rotation one would require to convert between the true and estimated rotation. This can be given by the unitary rotation operator

$$R(\Delta_i, \mathbf{u}_i) \equiv R(\boldsymbol{\Omega}_i)^\dagger R(\widehat{\boldsymbol{\Omega}}_i). \quad (26)$$

We need not worry about the direction \mathbf{u}_i in characterizing this error. To find Δ_i , we use the Hilbert-Schmidt norm $\text{Tr}[R(\boldsymbol{\Omega}_i)^\dagger R(\widehat{\boldsymbol{\Omega}}_i)] = \text{Tr}[R(\Delta_i, \mathbf{u}_i)] = \cos \Delta_i J + \sin \Delta_i J / \tan(\Delta_i/2)$, found using invariance of the trace under unitary transformations such that the trace is evaluated in the basis of eigenstates of $\mathbf{J} \cdot \mathbf{u}_i$, and solve for the smallest value of Δ_i . In doing so, we find the average deviations $\Delta = 0.54 \pm 0.43$ and $\Delta = 0.52 \pm 0.31$ for $J = 2$ and $J = 3$, respectively, with all of the values plotted in Fig. 4; the large ranges in deviations seem to signify that the algorithm is better for rotation angles close to 0 and 2π . Angular sensitivity can be further improved by encoding angle and axis using two or more King states that can be transformed into each other by a known rotation. This tends to average out some of the unavoidable systematic errors present in the experiment. In particular, using triples

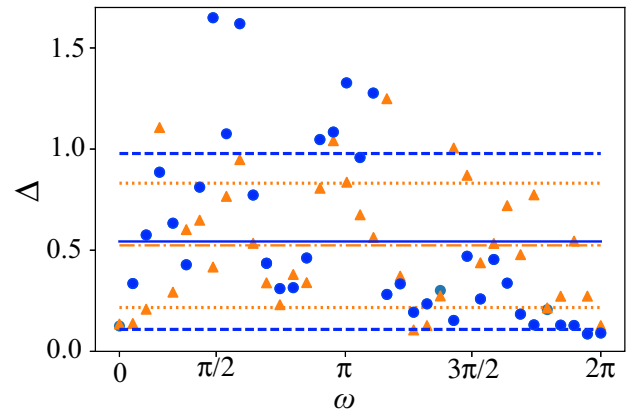


FIG. 4. Angular deviation between the true rotation and estimated rotation when all three parameters of the rotation are simultaneously estimated (all plotted in radians). The probe states are a King state with $J = 2$ (i.e., a state with tetrahedral symmetry; blue circles) and $J = 3$ (i.e., an octahedral state with $Z_2 \times S_4$ symmetry; orange triangles). There are 37 different experiments, each with the same to-be-determined axis of rotation and all rotation angles equally spaced from 0 to 2π . The mean is plotted as the solid (dot-dashed) line and the one standard deviation away as the dashed (dotted) lines for $J = 2$ ($J = 3$). The small errors, especially for rotation angles close to 0 and 2π , validate this method for estimating all three parameters of a rotation.

of King states separated by $\pi/6$ rotations we obtained deviations $\Delta = 0.23 \pm 0.1$ and $\Delta = 0.22 \pm 0.08$ for $J = 2$ and $J = 3$, which means improvement by a factor of more than 2. These deviations are all much smaller than might be found for a random rotation, where a random rotation would have deviation $\pi/2$ on average, showcasing the usefulness of our method.

VI. CONCLUDING REMARKS

Rotations constitute the epitome of how quantum properties can boost sensitivity and precision. We have demonstrated a simple measurement scheme that achieves results close to the ultimate bounds dictated by quantum theory, without requiring complicated and fragile entangled measurement strategies, and for simultaneously estimating all three parameters of a rotation. This proof of principle used MPLCs, which offer a range of advantages, including compactness, versatility, high efficiency, flexibility, cost effectiveness, and real-time adaptability. Nonetheless, the method is also sufficiently broad to apply to any other rotation-sensing application, so we expect these results to be relevant in years to come and believe they inspire research into performing coherent-state projections for a variety of physical systems.

ACKNOWLEDGMENTS

M.E. acknowledges support from the Academy of Finland through the project BIQOS (Decision 336375). A.Z.G. and F.B. acknowledge that the NRC headquarters is located on the traditional unceded territory of the Algonquin Anishinaabe and Mohawk people and support from NRC's Quantum Sensors Challenge Program. A.Z.G. acknowledges funding from the NSERC PDF program. M.H. acknowledges the Doctoral School of Tampere University and the Magnus Ehrnrooth Foundation. L.L.S.S. acknowledges support from Ministerio de Ciencia e Innovación (Grant PID2021-127781NB-I00). R.F. acknowledges support from the Academy of Finland through the Academy Research Fellowship (Decision 332399). M.E., M.H., R.F. acknowledge the support of the Academy of Finland through the Photonics Research and Innovation Flagship (PREIN—decision 320165).

Applications of Squeezed States in Interferometric Tests of General Relativity, p. 106.

- [5] M. Cerdonio, G. A. Prodi, and S. Vitale, Dragging of inertial frames by the rotating earth: Proposal and feasibility for a ground-based detection, *Gen. Rel. Grav.* **20**, 83 (1988).
- [6] I. Ciufolini, E. Pavlis, F. Chieppa, E. Fernandes-Vieira, and J. Pérez-Mercader, Test of general relativity and measurement of the Lense-Thirring effect with two earth satellites, *Science* **279**, 2100 (1998).
- [7] G. Zhanshe, C. Fucheng, L. Boyu, C. Le, L. Chao, and S. Ke, Research development of silicon MEMS gyroscopes: A review, *Microsyst. Technol.* **21**, 2053 (2015).
- [8] H. C. Lefèvre, *The Fiber-Optic Gyroscope* (Artech House, Norwood, MA, 2014), 2 ed.
- [9] V. M. Agafonov, A. V. Neeshpapa, and A. S. Shabalina, in *Encyclopedia of Earthquake Engineering*, edited by M. Beer, I. A. Kougioumtzoglou, E. Patelli, and I. S.-K. Au (Springer, Berlin, 2014), p. 1–19.
- [10] R. Leugoud and A. Kharlamov, Second generation of a rotational electrochemical seismometer using magnetohydrodynamic technology, *J. Seismol.* **16**, 587 (2012).
- [11] A. Cusano, D. L. Zaitsev, V. M. Agafonov, E. V. Egorov, A. N. Antonov, and V. G. Krishtop, Precession azimuth sensing with low-noise molecular electronics angular sensors, *J. Sensors* **2016**, 6148019 (2016).
- [12] W. W. Chow, J. Gea-Banacloche, L. M. Pedrotti, V. E. Sanders, W. Schleich, and M. O. Scully, The ring laser gyro, *Rev. Mod. Phys.* **57**, 61 (1985).
- [13] R. Anderson, H. R. Bilger, and G. E. Stedman, “sagnac”effect: A century of Earth-rotated interferometers, *Am. J. Phys.* **62**, 975 (1994).
- [14] T. L. Gustavson, A. Landragin, and M. A. Kasevich, Rotation sensing with a dual atom-interferometer Sagnac gyroscope, *Classical Quantum Gravity* **17**, 2385 (2000).
- [15] D. S. Durfee, Y. K. Shaham, and M. A. Kasevich, Long-Term Stability of an Area-Reversible Atom-Interferometer Sagnac Gyroscope, *Phys. Rev. Lett.* **97**, 240801 (2006).
- [16] D. Savoie, M. Altorio, B. Fang, L. A. Sidorenkov, R. Geiger, and A. Landragin, Interleaved atom interferometry for high-sensitivity inertial measurements, *Sci. Adv.* **4**, eaau7948 (2018).
- [17] C. L. Degen, F. Reinhard, and P. Cappellaro, Quantum sensing, *Rev. Mod. Phys.* **89**, 035002 (2017).
- [18] M. Szczykulska, T. Baumgratz, and A. Datta, Multiparameter quantum metrology, *Adv. Phys. X* **1**, 621 (2016).
- [19] J. S. Sidhu and P. Kok, Geometric perspective on quantum parameter estimation, *AVS Quantum Sci.* **2**, 014701 (2020).
- [20] F. Albarelli, M. Barbieri, M. G. Genoni, and I. Gianani, A perspective on multiparameter quantum metrology: From theoretical tools to applications in quantum imaging, *Phys. Lett. A* **384**, 126311 (2020).
- [21] E. Polino, M. Valeri, N. Spagnolo, and F. Sciarrino, Photonic quantum metrology, *AVS Quantum Sci.* **2**, 024703 (2020).
- [22] R. Demkowicz-Dobrzański, W. Górecki, and M. Guță, Multi-parameter estimation beyond quantum Fisher information, *J. Phys. A: Math. Theor.* **53**, 363001 (2020).
- [23] G. Björk, A. B. Klimov, P. de la Hoz, M. Grassl, G. Leuchs, and L. L. Sánchez-Soto, Extremal quantum states and their Majorana constellations, *Phys. Rev. A* **92**, 031801 (2015).

-
- [1] M. S. Grewal, A. P. Andrews, and C. G. Bartone, *Global Navigation Satellite Systems, Inertial Navigation, and Integration* (Wiley, Hoboken, 2013), 3 ed.
 - [2] A. Lawrence, *Modern Inertial Technology: Navigation, Guidance, and Control* (Springer, New York, 1998).
 - [3] G. E. Stedman, Ring-laser tests of fundamental physics and geophysics, *Rep. Prog. Phys.* **60**, 615 (1997).
 - [4] G. Leuchs and M. W. Hamilton, *Frontiers in quantum optics* (Adam Hilger, Bristol, 1986), Chap. Possible

- [24] G. Björk, M. Grassl, P. de la Hoz, G. Leuchs, and L. L. Sánchez-Soto, Stars of the quantum universe: extremal constellations on the Poincaré sphere, *Phys. Scr.* **90**, 108008 (2015).
- [25] A. Z. Goldberg, and D. F. V. James, Quantum-limited Euler angle measurements using anticoherent states, *Phys. Rev. A* **98**, 032113 (2018).
- [26] J. Zimba, “Anticoherent” spin states via the Majorana representation, *EJTP* **3**, 143 (2006).
- [27] E. Majorana, Atomi orientati in campo magnetico variabile, *Nuovo Cimento* **9**, 43 (1932).
- [28] P. de la Hoz, A. B. Klimov, G. Björk, Y. H. Kim, C. Müller, C. Marquardt, G. Leuchs, and L. L. Sánchez-Soto, Multipolar hierarchy of efficient quantum polarization measures, *Phys. Rev. A* **88**, 063803 (2013).
- [29] P. de la Hoz, G. Björk, A. B. Klimov, G. Leuchs, and L. L. Sánchez-Soto, Unpolarized states and hidden polarization, *Phys. Rev. A* **90**, 043826 (2014).
- [30] A. Z. Goldberg, P. de la Hoz, G. Björk, A. B. Klimov, M. Grassl, G. Leuchs, and L. L. Sánchez-Soto, Quantum concepts in optical polarization, *Adv. Opt. Photonics* **13**, 1 (2020).
- [31] F. Bouchard, P. de la Hoz, G. Björk, R. W. Boyd, M. Grassl, Z. Hradil, E. Karimi, A. B. Klimov, G. Leuchs, J. Řeháček, and L. L. Sánchez-Soto, Quantum metrology at the limit with extremal Majorana constellations, *Optica* **4**, 1429 (2017).
- [32] H. Ferretti, Ph.D. thesis, University of Toronto (2022), <https://hdl.handle.net/1807/110740>.
- [33] A. Z. Goldberg, A. B. Klimov, G. Leuchs, and L. L. Sánchez-Soto, Rotation sensing at the ultimate limit, *J. Phys.: Photonics* **3**, 022008 (2021).
- [34] J.-F. Morizur, L. Nicholls, P. Jian, S. Armstrong, N. Treps, B. Hage, M. Hsu, W. Bowen, J. Janousek, and H.-A. Bachor, Programmable unitary spatial mode manipulation, *J. Opt. Soc. Am. A* **27**, 2524 (2010).
- [35] P. Boucher, A. Goetschy, G. Sorelli, M. Walschaers, and N. Treps, Full characterization of the transmission properties of a multi-plane light converter, *Phys. Rev. Res.* **3**, 023226 (2021).
- [36] E. W. Grafarend and W. Kühnel, A minimal atlas for the rotation group $so(3)$, *Int. J. Geomath.* **2**, 113 (2011).
- [37] J. F. Cornwell, *Group Theory in Physics* (Academic, New York, 1984), Vol. II.
- [38] P. Jordan, Der Zusammenhang der symmetrischen und linearen Gruppen und das Mehrkörperproblem, *Z. Phys.* **94**, 531 (1935).
- [39] J. Schwinger, in *Quantum Theory of Angular Momentum*, edited by L. C. Biedenharn and H. Dam (Academic, New York, 1965).
- [40] S. Chaturvedi, G. Marmo, and N. Mukunda, The Schwinger representation of a group: Concept and applications, *Rev. Math. Phys.* **18**, 887 (2006).
- [41] H. Bacry, *Group Theory and Constellations* (Publibook, Paris, 2004).
- [42] I. Bengtsson and K. Życzkowski, *Geometry of Quantum States* (Cambridge University, Cambridge, 2017).
- [43] A. Perelomov, *Generalized Coherent States and Their Applications* (Springer, Berlin, 1986).
- [44] J. P. Gazeau, *Coherent States in Quantum Physics* (Wiley-VCH, Manheim, 2009).
- [45] J. P. Dowling, Quantum optical metrology—the lowdown on high-N00N states, *Contemp. Phys.* **49**, 125 (2008).
- [46] C. W. Helstrom, *Quantum Detection and Estimation Theory* (Academic, New York, 1976).
- [47] S. M. Kay, *Fundamentals of Statistical Signal Processing* (Prentice Hall, Upper Saddle River, 1993), Vol. 1.
- [48] S. L. Braunstein and C. M. Caves, Statistical Distance and the Geometry of Quantum States, *Phys. Rev. Lett.* **72**, 3439 (1994).
- [49] A. Z. Goldberg, L. L. Sánchez-Soto, and H. Ferretti, Intrinsic Sensitivity Limits for Multiparameter Quantum Metrology, *Phys. Rev. Lett.* **127**, 110501 (2021).
- [50] D. Šafránek, Simple expression for the quantum Fisher information matrix, *Phys. Rev. A* **97**, 042322 (2018).
- [51] F. Bouchard, N. H. Valencia, F. Brandt, R. Fickler, M. Huber, and M. Malik, Measuring azimuthal and radial modes of photons, *Opt. Express* **26**, 31925 (2018).
- [52] K. Husimi, Some formal properties of the density matrix, *Proc. Phys. Math. Soc. Jpn.* **22**, 264 (1940).
- [53] B. Hofmann-Wellenhof, H. Lichtenegger, and J. Collins, *Global Positioning System* (Springer, Vienna, 2001).
- [54] A. Jesacher, A. Schwaighofer, S. Fürhapter, C. Maurer, S. Bernet, and M. Ritsch-Marte, Wavefront correction of spatial light modulators using an optical vortex image, *Opt. Express* **15**, 5801 (2007).
- [55] E. Bolduc, N. Bent, E. Santamato, E. Karimi, and R. W. Boyd, Exact solution to simultaneous intensity and phase encryption with a single phase-only hologram, *Opt. Lett.* **38**, 3546 (2013).
- [56] S. Z. D. Plachta, M. Hiekkämäki, A. Yakaryılmaz, and R. Fickler, Quantum advantage using high-dimensional twisted photons as quantum finite automata, *Quantum* **6**, 752 (2022).
- [57] M. Hiekkämäki, R. F. Barros, M. Ornigotti, and R. Fickler, Observation of the quantum Gouy phase, *Nat. Photonics* **16**, 1 (2022).
- [58] G. Labroille, B. Denolle, P. Jian, P. Genevaux, N. Treps, and J.-F. Morizur, Efficient and mode selective spatial mode multiplexer based on multi-plane light conversion, *Opt. Express* **22**, 15599 (2014).
- [59] F. Brandt, M. Hiekkämäki, F. Bouchard, M. Huber, and R. Fickler, High-dimensional quantum gates using full-field spatial modes of photons, *Optica* **7**, 98 (2020).
- [60] N. K. Fontaine, R. Ryf, H. Chen, D. T. Neilson, K. Kim, and J. Carpenter, Laguerre-Gaussian mode sorter, *Nat. Commun.* **10**, 1 (2019).
- [61] Z. Hradil, D. Mogilevtsev, and J. Řeháček, Biased Tomography Schemes: An Objective Approach, *Phys. Rev. Lett.* **96**, 230401 (2006).
- [62] J. Řeháček, D. Mogilevtsev, and Z. Hradil, Tomography for quantum diagnostics, *New J. Phys.* **10**, 043022 (2008).